Supporting information: Plasmon-enhanced Raman scattering by carbon nanotubes optically coupled with near-field cavities

Sebastian Heeg,[*,†,‡] Antonios Oikonomou,[¶,§] Roberto Fernandez-Garcia,[‖] Christian Lehmann,[†] Stefan A.Maier,[‖] Aravind Vijayaraghavan,[‡,§] and Stephanie Reich[†]

Department of Physics, Freie Universität Berlin, 14195 Berlin, Germany, School of Materials, The University of Manchester, Manchester M13 9PL, U.K., School of Computer Science, The University of Manchester, Manchester M13 9PL, U.K., Centre for Mesoscience and Nanotechnology, The University of Manchester, Manchester M13 9PL, U.K., and Department of Physics, Imperial College London, London SW7 2AZ, U.K.

E-mail: sebastian.heeg@manchester.ac.uk

[*]To whom correspondence should be addressed
[†]Department of Physics, Freie Universität Berlin, 14195 Berlin, Germany
[‡]School of Materials, The University of Manchester, Manchester M13 9PL, U.K.
[¶]School of Computer Science, The University of Manchester, Manchester M13 9PL, U.K.
[§]Centre for Mesoscience and Nanotechnology, The University of Manchester, Manchester M13 9PL, U.K.
[‖]Department of Physics, Imperial College London, London SW7 2AZ, U.K.

Contents

S1 Dielectrophoretic deposition of CNTs and yields

Using unsorted carbon nanotubes as the starting material, we successfully placed carbon nanotube bundles in plasmonic cavities. The deposition of an individual tube has not been observed so far. This is not surprising; the higher the polarizability of an object, the more likely it is to be deposited. From a pristine CNT solution, bundles will be deposited first, followed by metallic and finally semiconducting tubes[1,2] Depending on the desired configuration an adequate, pre-sorted starting material may be chosen to deposit single carbon nanotubes.

The presence of nanoplasmonic antennas, e.g., metallic nano structures, placed between an electrode pair influences the field distribution during dielectrophoretic deposition.[3] To quantify possible effects on the deposition efficiency, only every second electrode pair within an array contains plasmonic antennas (arrows), as shown in Figure S1(a). Structural characterization of many locations showed that the plasmonic antennae in the electrode gap do not affect the nanotube assembly.

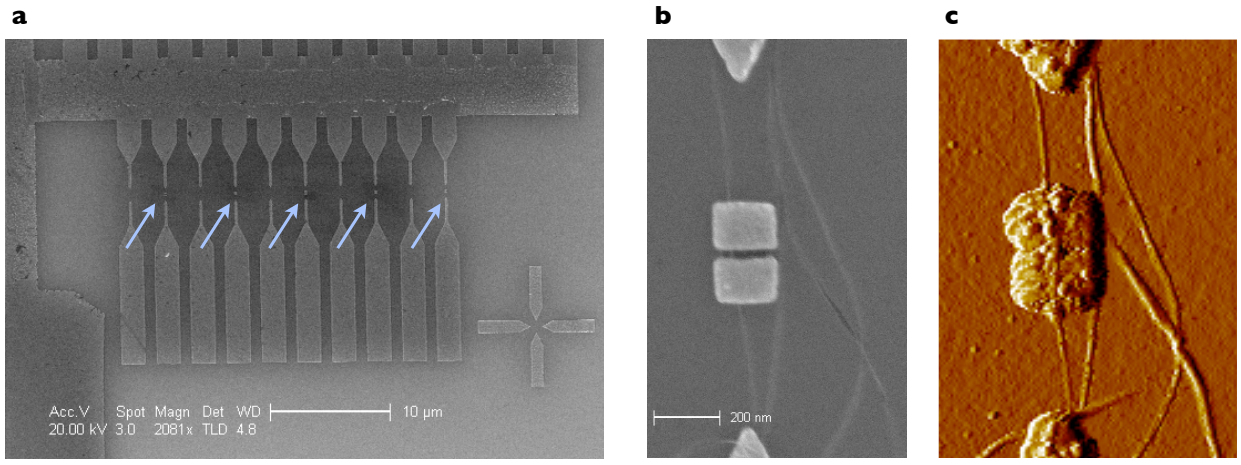

Figure S1: (a) SEM imagine of array with plasmonic structures placed between every second pair of electrodes (arrows). (b) SEM image of a carbon nanotube suspended over a cavity formed by rods and additional nanotubes close by. (c) same location as in (b) imagined per AFM (error signal).

We use atomic force microscopy (AFM) to characterize plasmonic antennas interfaced with carbon nanotubes to avoid damage to carbon nanotubes and the deposition of hydrocarbons by scanning electron microscopy (SEM). Figure S1 compares a location characterized with SEM, Figure S1(b), and AFM(c). While features like the gap between the rods and sharp edges are poorly reproduced in Figure S1(c), characterization by AFM is sufficient to observe carbon nanotubes suspended over a cavity, its presence on top of a particle and to detect additional nanotubes in the vicinity of the nano structure [compare main paper, Figure 1(c)-(e)].

The yield for CNTs deposited inside nanodisk dimer cavities - such as CNT-B and CNT-R - was 3%, equivalent to four out of 135 devices on the sample. All four nanotubes showed features of plasmonic enhancement, see Sect. S4.5. We expect this yield to increase upon optimizing the deposition parameters. The deposition yield for the alternative interfaces, shown in Figure 1 of the main manuscript, was significantly higher: For 21.7% of the gapped double rod structures (see main paper, Figure 1(b)), at least one carbon nanotube crossed the corresponding gap. The dielectrophoretic deposition was optimized for this interface type. For 13.3% of the single nano disks (see main paper, Figure 1(c)), at least one nanotube crossed the top surface. For 23.7% of the dimer structures comparable to CNT-B (see main paper, Figure 1(e)), at least one nanotube crossed the top surface of one of the two nano disks. None of the alternative interfaces showed prominent features of enhancement, which we discuss in Sect. S 4.5.

S2 Near-field simulations

Figure S2(a) depicts the simulated spatial distribution of the near-field enhancement $|E/E_0|^2$ of the dimer structure for P_y. The near-field in the plasmonic cavity is polarized along the y-direction. The corresponding component $|E_y/E_0|^2$ is shown in Figure S2(b). Near-field components polarized along the x-direction, Figure S2(c), and z-direction, Figure S2(d), are present in the very vicinity of the nano disk edges, but not in the cavity. The overall intensity of the x and z near-field components are very low compared to the dominating component $|E_y/E_0|^2$ polarized along y.

Figure S2(e-h) shows the corresponding near-field components for P_x. The enhancement drops by an order of magnitude compared to P_y. No enhanced near-field components are present in the cavity.

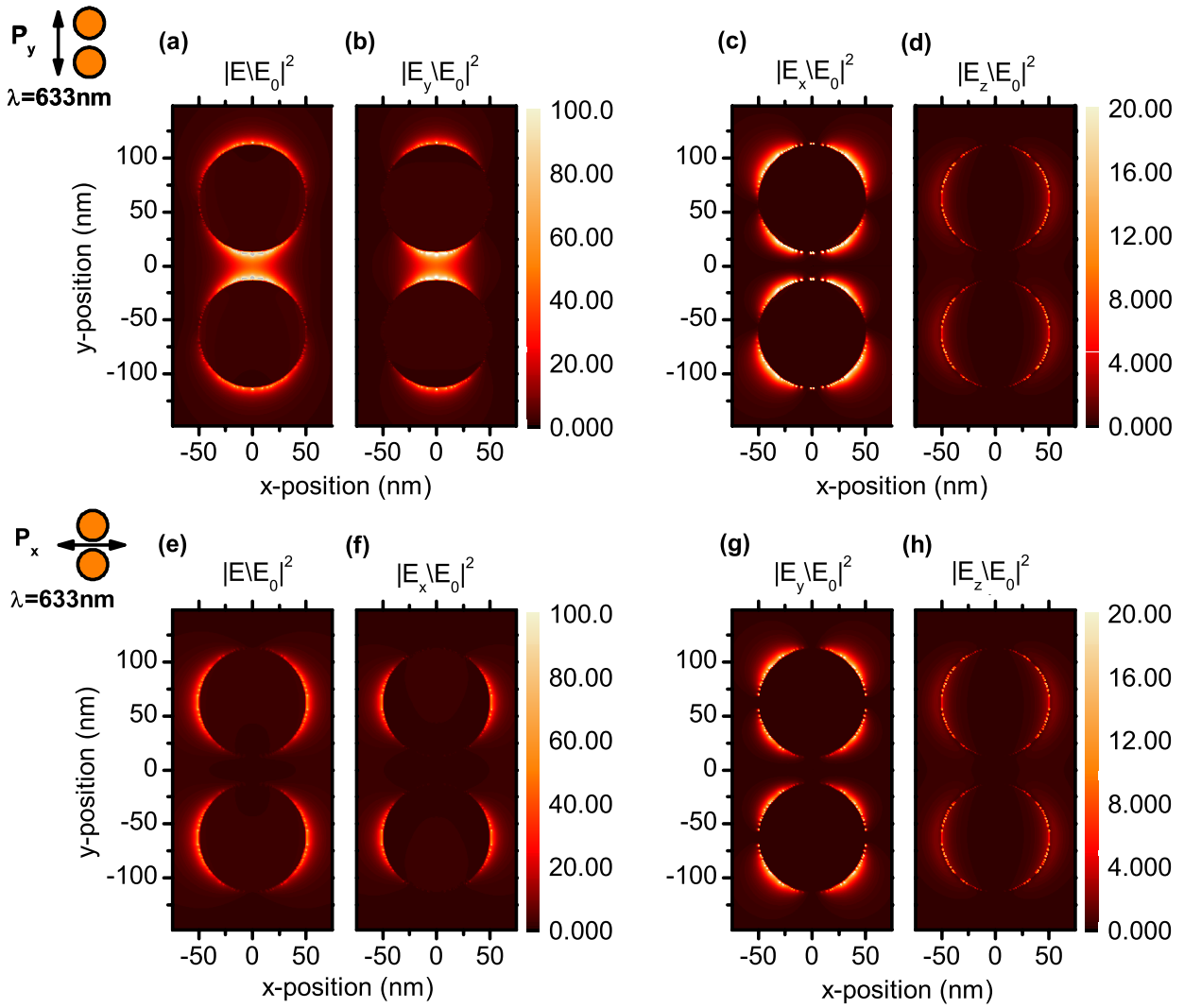

Figure S2: (a) Spatial distribution of the near field enhancement $|E/E_0|^2$ for P_y. The corresponding components polarized along $y-$, $x-$, and $z-$ axes are shown in (b)-(d), respectively. (e) spatial distribution of the near field enhancement $|E/E_0|^2$ for P_x. The corresponding components polarized along $x-$, $y-$, and $z-$ axes are shown in (f)-(h), respectively. All simulations are evaluated at z= 3nm above the substrate for an excitation of $\lambda = 633$nm.

S3 Raman scattering of carbon nanotubes

S3.1 Phonon symmetries and selection rules

A quasi particle like an electron or a phonon in carbon nanotubes is characterized by a set of quantum numbers (m,k). The continous linear momentum k corresponds to wave vectors along the carbon nanotube axis; the quasi angular momentum m represents the confinement around the circumference of a nanotube and takes integer values, see Refs. [4-6] for details.

Phonons of carbon nanotubes are obtained by symmetry considerations using the nanotube line group formalism.[4] The Raman active phonons in carbon nanotubes belong to the three symmetries,[5,6] which we assign with their corresponding m quantum number:

$$A_{1(g)}, m = 0 \qquad E_{1(g)}, m = \pm 1 \qquad E_{2(g)}, m = \pm 2$$

The subscript g in parentheses applies to achiral (zig-zag and armchair) nanotubes, which posses a higher symmetry than chiral nanotubes. With few exceptions, m is a fully conserved quantum number in carbon nanotubes. It offers a quick way to work out the selection rules for first order scattering of Γ-point (phonon wave vector $\mathbf{q} = 0$) phonons in the visible.[5–7] The conservation of m defines the polarization of the incident and scattered light and the electronic transition involved in the Raman process of each of the phonon symmetries.

In accordance with carbon nanotube metrology, the axis of the nanotube corresponds the z-axis. An optical transition polarized along z conserves the quasi angular momentum $\Delta m = 0$.[5] If both the incident and scattered light are polarized along z - expressed as (z,z) - the quasi angular momentum remains unchanged in every step of the Raman process. Only $A_{1(g)}$ phonons with $m = 0$ are allowed in this configuration. The $A_{1(g)}$ phonons are the radial breathing mode and two G-modes (one for achiral tubes) observed in carbon nanotube Raman spectra.[6] The optical transitions occur between electronic states of equal quasi-angular momentum, commonly labelled E_{ii}.

For an optical transition polarized perpendicular to the tube axis, e.g., along x, $\Delta m = \pm 1$.[5] If the outgoing light is polarized along z - realizing a (x,z) configuration in the Porto notation - the

photonics part of the Raman process yields $\Delta m = \pm 1$. Only $E_{1(g)}$ phonons with $\Delta m = \pm 1$ conserve the total quasi angular momentum. The corresponding optical transition $E_{i,i\pm 1}$ occur between states of different m, e.g., E_{12} and E_{23}. Similar to the G-modes of $A_{1(g)}$ symmetry, two $E_{1(g)}$ modes are closely related to the longitudinal and transversal optical phonons in graphene and occur in the range of $1500-1600\,\mathrm{cm}^{-1}$ as well.

In an (x,x) configuration, where both the incident and the scattered light are polarized perpendicular to the tube axis, the photonic part delivers either $\Delta m = \pm 2$ or $\Delta m = 0$. Hence phonon scattering either arises from $A_{1(g)}$ phonons with $m = 0$ or $E_{2(g)}$ phonons with $m = \pm 2$. Similar to $E_{1(g)}$ type vibrations, the phonons of $E_{2(g)}$ symmetry are expected in the range of $1500-1600\mathrm{cm}^{-1}$. There are also low-frequency vibrations with $E_{1(g)}$ and $E_{2(g)}$ symmetry. They are expected between ~ 50 and $400\mathrm{cm}^{-1}$, but have never been convincingly demonstrated.

We summarize the selection rules for Raman scattering in carbon nanotubes including the optical transitions in Table S1. For $E_{1(g)}$ and $E_{2(g)}$ phonons, incoming and outgoing resonances (see main paper) belong to states of different quasi angular momentum m. Examples for each scattering configuration are listed in Table S1. Due to the antenna effect, only $A_{1(g)}$ phonons in (z,z) configuration are observed, while the Raman intensity for all other scattering configurations vanishes as discussed in the main paper. More detailed information is can be found for instance in Refs. 6 and 7. An alternative and very intuitive representation was introduced by *Jorio et al.*[8,9]

.

Table S1: Scattering configuration including the phonons and optical transitions involved in the process. Configurations like (x,y) are omitted, as the do not occur in backscattering geometry.

scattering configuration	phonon symmetry	(incoming/outgoing) resonances	comment
(z,z)	$A_{1(g)}$, $\Delta m = 0$	(E_{11}/E_{11}), (E_{22}/E_{22}), (E_{33}/E_{33}),..	RBM, 2 G-modes
$(x,z),(y,z)$	$E_{1(g)}$, $\Delta m = \pm 1$	(E_{12}/E_{11}), (E_{21}/E_{11}), (E_{23}/E_{22}),..	surpressed
$(z,x),(z,y)$	$E_{1(g)}$, $\Delta m = \pm 1$	(E_{11}/E_{21}), (E_{22}/E_{12}), (E_{22}/E_{32}),..	surpressed
$(x,x),(y,y)$	$A_{1(g)}$, $\Delta m = 0$	(E_{12}/E_{21}), (E_{21}/E_{12}), (E_{23}/E_{32}),..	surpressed
$(x,x),(y,y)$	$E_{2(g)}$, $\Delta m = \pm 2$	(E_{21}/E_{32}), (E_{23}/E_{12}),..	surpressed

S3.2 Fully symmetric vibrations, their Raman tensor and angle-dependent Raman intensities

The Raman tensor of $A_{1(g)}$ vibrations such as the G- and Radial breathing modes in carbon nanotube is of diagonal[7] form

$$\mathscr{R} = \begin{pmatrix} \alpha_{\perp}^{R} & 0 & 0 \\ 0 & \alpha_{\perp}^{R} & 0 \\ 0 & 0 & \alpha_{\parallel}^{R} \end{pmatrix}, \tag{1}$$

where $\alpha_{\perp}^{R}$ denotes the perpendicular and $\alpha_{\parallel}^{R}$ the parallel Raman polarizability with respect to the nanotube axis. The anisotropic polarizability of carbon nanotubes can be expressed via the depolarization matrix $\mathbf{d}$ that relates the Raman excitation field E to an external driving field E_0 as[10]

$$E = \mathbf{d}\,E_0 = \frac{1}{\alpha_{\parallel}^{0}} \begin{pmatrix} \alpha_{\perp}^{0}(1+\alpha_{\perp}^{0}/4\pi\varepsilon_0 r^2) & 0 & 0 \\ 0 & (1+\alpha_{\perp}^{0}/4\pi\varepsilon_0 r^2) & 0 \\ 0 & 0 & \alpha_{\parallel}^{0} \end{pmatrix}, \tag{2}$$

where $\alpha_{\perp}^{0}$ denotes the unscreened transverse optical polarizabilty, $\alpha_{\parallel}^{0}$ denotes the parallel optical polarizabilty and r denotes the radius of the carbon nanotube in Angstrom. The Raman intensity I_R is expressed as

$$I_{\mathscr{R}} = |\vec{e}_s \cdot \mathscr{R} \cdot \vec{e}_i|^2, \tag{3}$$

where $\vec{e}_i$ and $\vec{e}_s$ denote the polarization of the incident and scattered light, respectively. For carbon nanotubes, it is impossible to distinguish experimentally between optical polarizability ($\alpha_{\parallel,\perp}^{R}$) and Raman polarizability ($\alpha_{\parallel,\perp}^{0}$). Therefore we define an effective Raman tensor $\mathscr{R}_{\text{eff}} = \text{diag}(\alpha_{\perp}, \alpha_{\perp}, \alpha_{\parallel})$, that includes both quantities. As introduced in Section S3, the axis of the carbon nanotubes is defined as the z-component. To describe the relative orientation of both the plasmonic dimer and the polarization of the incident light relative to the tube axis, we rotate the polarization of incident and scattered light accordingly. The angle dependent Raman intensity for parallel

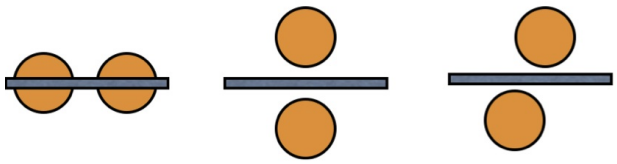

$\phi = 0$ $\phi = 90$ $\phi = 75$

Figure S3: Rotation of plasmonic dimer and incident light polarization to match the nanotube orientation of CNT-B observed in the experiment.

polarization of the incoming and scattered light is therefore given by

$$\begin{aligned} I_{\mathscr{R}}(\phi) &\propto |\vec{e}_s \cdot \mathscr{R}_{\text{eff}} \cdot \vec{e}_i|^2 \\ &= \left| \begin{pmatrix} 0 \\ \sin\phi \\ \cos\phi \end{pmatrix} \begin{pmatrix} \alpha_\perp & 0 & 0 \\ 0 & \alpha_\perp & 0 \\ 0 & 0 & \alpha_\parallel \end{pmatrix} \begin{pmatrix} 0 \\ \sin\phi \\ \cos\phi \end{pmatrix} \right|^2 \\ &= \alpha_\perp^2 \sin^4\phi + 2\alpha_\perp \alpha_\parallel \cos^2\phi \sin^2\phi + \alpha_\parallel^2 \cos^4\phi, \end{aligned} \tag{4}$$

where ϕ denotes the angle between the axis of the plasmonic dimer and the carbon nanotubes as depicted in Figure S3. For $\alpha_\parallel \gg \alpha_\perp$, as it is the case in Raman scattering in carbon nanotubes, only the Cos^4-term is relevant.

S3.3 Raman intensity of CNT-B

In the following we determine the enhancement factor that the cavity itself F_{cav} has to deliver in order to obtain the experimentally observed signal enhancement F_{exp}. It is given by the ratio of F_{exp} and the angle dependent intrinsic Raman response $I_{\mathscr{R}}(\phi)$ as

$$F_{\text{cav}} = \frac{F_{\text{exp}}}{I_{\mathscr{R}}(\phi)}. \tag{5}$$

For CNT-B, F_{exp} is given by the product of $G(P_y)/G(G_x) \sim 30$ for an excitation at 633 nm and the factor arising from the localization of the signal ~ 8.8, which yields $F_{\text{exp}} \sim 264$. We insert these

values in Eq. (5) using Eq. (4) and list the corresponding cavity enhancement factors in Table S2.

The relative values for the polarizabilities $\alpha_\perp$ and $\alpha_\parallel$ have to be understood as a rudimental framework and represent the range of exemplary cases present in the literature. The absolute numbers strongly depend on the nanotube chirality, radius, excitation energy (and its proximity to an optical transition), isolated or bundles nanotubes and whether the calculations are performed in a static approximation or dynamic processes are included.[10–12] In addition, the Raman polarizibilities introduced in Eq. (1) are not known. The important information of Table S2, however, are the trends in F_{cav} with changing input parameters. A decreasing ratio of $\alpha_\perp$ and $\alpha_\parallel$ increasingly takes into account the one-dimensional nature of carbon nanotubes. Experimentally, this results in (i) smaller experimental enhancements for $\phi = 90^\circ$ such as CNT-R and and (ii) increases the importance of rotating the plasmonic structure against the CNT-axis to increase the experimental enhancement. While this analysis cannot supply quantitative data for the real enhancement factor of the cavity at this stage, it provides conclusive arguments to explain the difference in the experimental enhancement factors for CNT-B and CNT-R and points towards cavity enhancement factors on the order of 10^4.

Table S2: Cavity enhancement factors necessary to match experimental values observed for CNT-B, for different ratios of $\alpha_\perp$ and $\alpha_\parallel$ and varying orientation of the nanotube relative to the dimer axis, compare Figure S3.

	$\phi = 0$	$\phi = 90$	$\phi = 75$
$\alpha_\perp = \frac{1}{3}\alpha_\parallel$	2.6×10^2	2.9×10^3	2.2×10^3
$\alpha_\perp = \frac{1}{10}\alpha_\parallel$	2.6×10^2	2.6×10^4	1.0×10^4
$\alpha_\perp = \frac{1}{30}\alpha_\parallel$	2.6×10^2	2.6×10^5	2.8×10^4

S4 Additional Raman data

S4.1 Raman spectra of CNT starting material

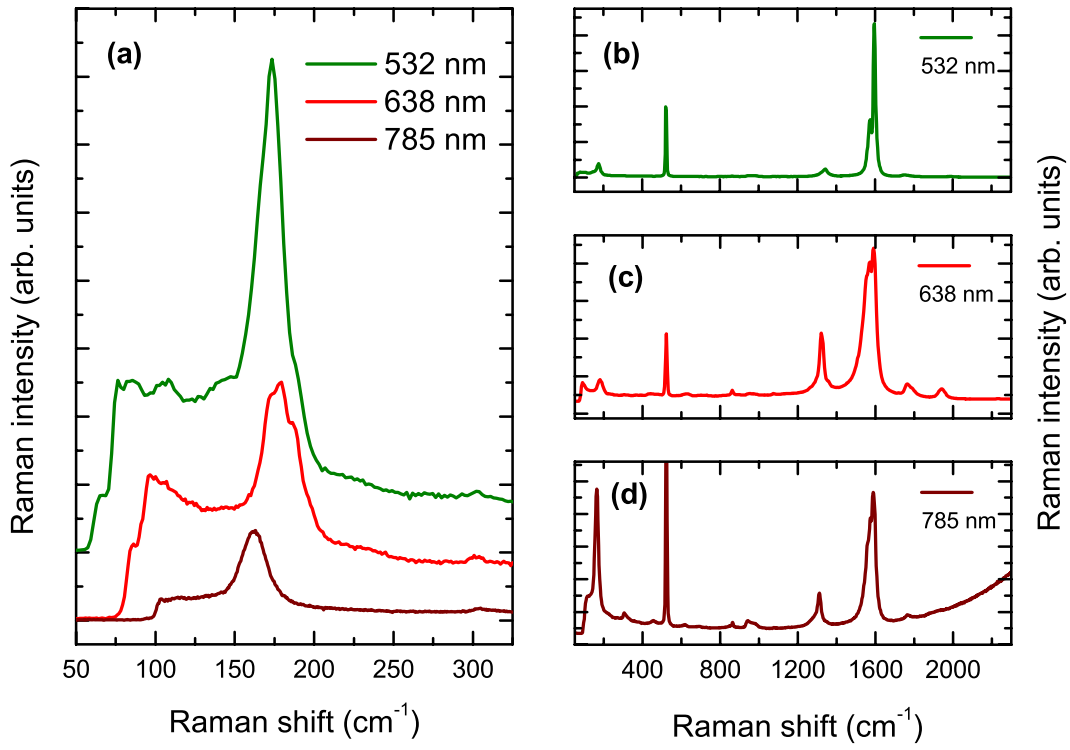

Figure S4: (a) Radial breathing modes of the starting material drop coated on a pristine SiO_2/Si substrate for different excitations wavelengths. Spectra including the D- and G-modes are shown for in (b, 532 nm), (c, 638 nm), and (d, 785 nm). They are normalized to the G-peak height.

CNT-starting material in solution was drop coated on a SiO_2/Si substrate. The Raman spectra in Figure S4 were acquired for excitation wavelengths of 532 nm, 638 nm, 785 nm using an single-grating Horiba Xplora spectrometer. From the RBM frequencies in Figure S4(a), we deduce that the SWCNTs present in the starting material have diameters between 1.3 nm and 1.6 nm.[13] For all excitations used in the experiment, we observe radial-breathing modes, G-peaks and defect-induced D-modes as shown in Figure S4(b-d). The broadened G-peak in (c) suggests that metallic carbon nanotubes dominate the Raman spectra for $\lambda = 638$ nm.

S4.2 G-mode comparison of the starting material and CNT-B

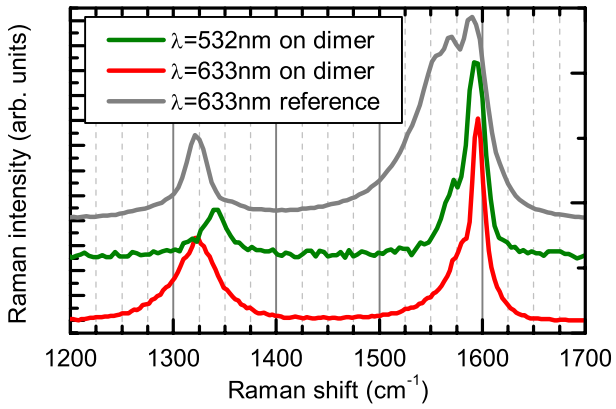

Figure S5: Comparison of G-and D-mode spectra of the starting material (grey, $\lambda = 633\,\text{nm}$), CNT-B in the presence of plasmonic enhancement (red, $\lambda = 633\,\text{nm}$) and without external enhancement (green, $\lambda = 532\,\text{nm}$). The spectra are scaled to the equal heights with respect to the G-peak.

Figure S5 compares the G-mode shapes of CNT-B (red, green; see main paper, Figure 4) with the starting material (grey) for an excitation of $\lambda = 633\,\text{nm}$. For the latter, the lower component of the G-mode is downshifted and broadened, indicating that metallic carbon nanotubes contribute to the Raman signal. This signature is missing for CNT-B. Most likely, the bundle forming CNT-B does not contain metallic carbon nanotubes, but only semiconducting tubes. The lack of a metallic G-mode shape is in agreement with our observation that the intrinsic response of CNT-B for an excitation of 633 nm is extremely weak or vanishes completely.

S4.3 Width of laser spot from Raman line scan

Figure S6 shows a Raman line scan crossing the dimer that we extracted from the Raman map of CNT-B (Main paper, Figure 3(d)). The integrated G-peak intensity is plotted against the x-axis within our laboratory frame, where $x = 0$ corresponds to the position of the dimer. The profile represents the folding of the laser spot with segments of CNT within the cavity subject to enhancement. A Gaussian fit (red) delivers a full width at half maximum of 440nm. Approximating the enhanced signals as a point like source yields a laser spot size of $\sim$ 880nm.

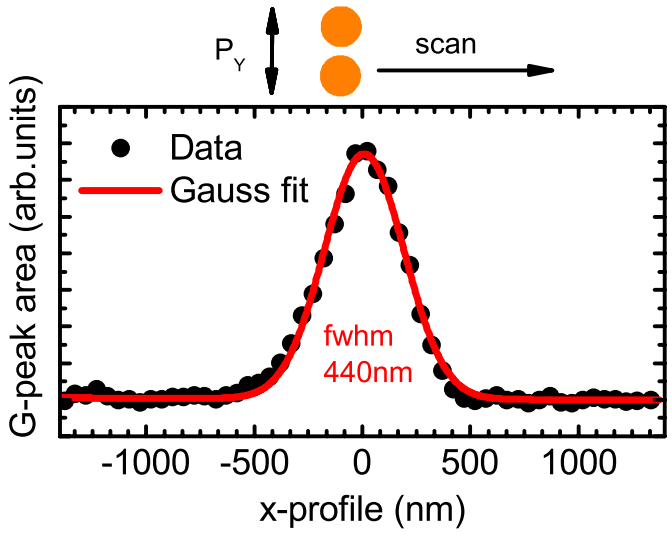

Figure S6: Spatial profile of integrated G-peak intensity of CNT-B crossing over the dimer along x for $\lambda = 633\,\text{nm}$ and P_Y. The step size of the scan was 50 nm.

S4.4 Characterization of CNT-R

Figure S7(a) and (b) depict spatial Raman maps of the integrated G-peak intensity of CNT-R for P_Y and P_X, respectively. Both maps were acquired with $\lambda = 633\,\text{nm}$. An AFM error image shown in (d) confirms that CNT-R is placed in the cavity formed by the two nano disks. For P_Y, where the cavity is in the "on" state, the signal is localized at the dimer as for CNT-B [main paper, Figure 3(e)]. The segments of CNT-R in the cavity dominate the Raman signal. While additional nanotubes are present in the vicinity of the dimer, some of which are oriented along the y-axis, their contribution to the Raman signal for P_Y is negligible. Otherwise, we would expect the Raman signature in Figure S7(a) to be broadened along the y-axis. The spatial Raman distribution for P_X represents the intrinsic response of CNT-R. Its spatial distribution follows the location of CNT-R. We observe the highest Raman intensity at the dimer location, where the overlap of the laserspot and CNT-R is maximal. In addition, minor plasmonic enhancement may occur for this polarization for the nanotubes or nanotube segments next to the nano disks along x.

The G-mode spectra at the dimer location are shown in Figure S7(c) and (d) for P_Y and P_X, respectively. While we observe small differences in the spectra, the general peak shape is retained and no evidence for additional modes is found. We attribute the small difference to additional nanotubes in the vicinity of the dimer, which are illuminated by the laser spot. Applying an analysis

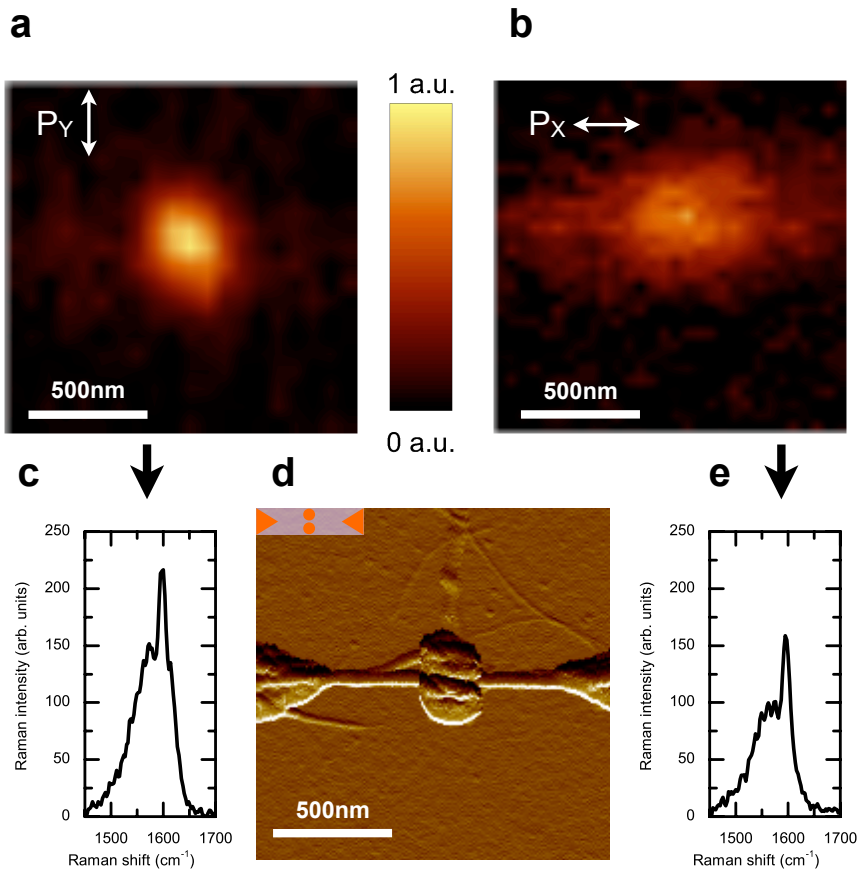

Figure S7: Raman maps of the integrated G-peak intensity of CNT-R for P_y (a) and P_x (b), taken with an excitation wavelength of 633 nm. The corresponding spectra taken on top of the dimer are presented in (c) and (e). (d) shows an AFM error image of CNT-R being placed in the cavity. Additional nanotubes are present in the vicinity of the nano disk dimer and the electrodes.

similar to CNT-B (see main paper), we arrive at an overall enhancement factor of the order of 10^2.

S4.5 Additional CNTs interfaced with dimer structures showing enhancement

We observed enhancement for all four nanotube bundles deposited directly in the dimer cavity (see Sect. S1 for a discussion of the DEP yield). In Table S3 we list the experimentally observed ratio P_Y/P_X of these structures. CNT-B and CNT-R were discussed in detail in the manuscript. For the two additional bundles (CNT S-1, CNT S-2) the orientation of the CNTs with respect to the cavity and the length of the nanotube segment subject to plasmonic enhancement is unknown. We observed indications of enhancement for several more devices, but no experimental values or enhancement factor could be extracted. This was due to the presence of additional CNTs in the immediate vicinity or a signal not fulfilling the threshold condition for enhancement which we define as $P_Y/P_X > 1$.

Out of the structures depicted in the main manuscript, only CNTs placed in dimer cavities showed enhancement for the excitation energies employed in our experiments (532 nm and 633 nm). We relate this to a missing or very small overlap of excitation energy and LSP resonances for the other structures. Further, for CNTs suspended across the gapped rod structures and nanotube on top of isolated nano disk, the means to confirm enhancement are limited to spatial mapping only: switching between plasmonic enhancement and the intrinsic CNT response via polarization is not possible, as both effects occur for the same polarization.

Table S3: Experimentally observed enhancement for several devices. Only for CNT-B and CNT-R, the orientation and position of the CNTs with respect to the cavity is known entirely. For the other devices that showed enhancement, the corresponding multiplicative factors arising from depolarization and localization are unknown.

	enhancement factor	experimental: P_Y/P_X	Φ
CNT-B	1.8×10^3	30	75°
CNT - SI - 1	–	4.6	–
CNT - SI - 2	–	1.8	–
CNT-R	8.8×10^2	1.5	90°
several	–	< 1	–

S5 Conductive AFM

As a proof of principle, we measure the current-voltage (IV)-characteristics of the carbon nanotube shown in Figure S8(a). Using a conductive AFM as schematically depicted in (b) allows us to individually address a floating electrode at a location of choice. The IV-curve of the nanotube shown in (a) are depicted in (d). The strong non-linear behavior indicates the presence of a Schottky barrier, which we attribute to the boundary formed between the AFM cantilever (coated with diamond) and the floating electrode. We isolate its contribution according to the diagram shown in Figure S8(b). The series resistance R represents the interfacial resistance of the bulk contact of the cantilever, the interfacial resistance between the electrode and the tube as well the intrinsic nanotube resistance. We use a simplified model[14] to separately fit the forward, Figure S8(e), and reverse bias sweep, Figure S8(f), as

$$I = I_0 \cdot \left(e^{\frac{V-IR}{V_T n}} - 1 \right).$$

I_0 represents the saturation current, $V_T = k_B T/q$ the thermal voltage, R the series resistance described above, and n the ideality factor. It is a measure for the quality of the diode under investigation for which $n = 1$ represents an ideal diode.

The contact resistance between the electrodes and the nanotube amounts to 174kΩ and 228kΩ, respectively. The difference between forward and reverse bias serves as a good indicator for the error of the model introduced above, which we estimate to be around 50kΩ. The order of magnitude of the resistance is in good agreement with literature values for carbon nanotubes deposited by dielectrophoresis.[15] We conclude that a good electric contact between the nanotube and the electrodes was established. This provides the technical framework to electrically access the interplay between carbon nanotubes and plasmonic cavities in future studies.

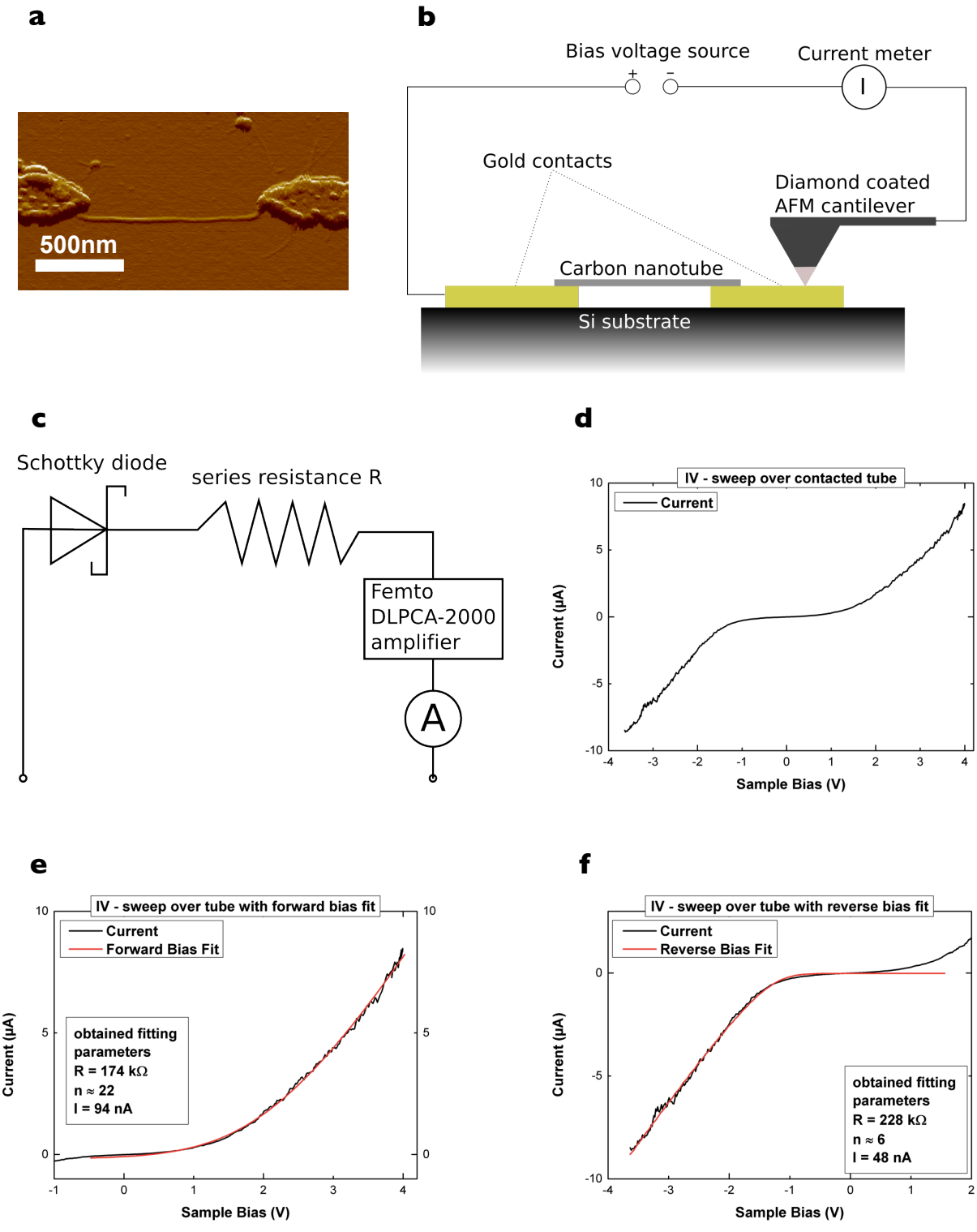

Figure S8: (a) AFM error image of a carbon nanotube connecting the two electrodes. (b), schematic of measurement setup where the floating electrode is connected via conductive AFM. The corresponding circuitry is schematically shown in (c). (d) I-V sweep for the nanotube shown in (a). Forward and reverse bias sweeps are fitted separately as shown in (e) and (f), respectively.

S6 Bibliography

References

1. Krupke, R.; Hennrich, F.; Weber, H. B.; Kappes, M. M.; von Löhneysen, H. *Nano Lett.* **2003**, *3*, 1019–1023.

2. Blatt, S.; Hennrich, F.; Löhneysen, H. v.; Kappes, M. M.; Vijayaraghavan, A.; Krupke, R. *Nano Lett.* **2007**, *7*, 1960–1966.

3. Marquardt, C. W.; Blatt, S.; Hennrich, F.; Löhneysen, H. v.; Krupke, R. *Appl. Phys. Lett.* **2006**, *89*, 183117.

4. Damnjanović, M.; Milošević, I.; Vukovic, T.; Sredanović, R. *Phys. Rev. B* **1999**, *60*, 2728–2739.

5. Damnjanović, M. *Phys. Lett. A* **1983**, *94*, 337–339.

6. Thomsen, C.; Reich, S. Raman scattering in carbon nanotubes. *Light Scattering in Solid IX: Novel Materials and Techniques*, Topics in Applied Physics, Vol. 108, edited by M. Cardona, (Springer Verlag, Heidelberger Platz 3, D-14197 Berlin, Germany, 2007), 115–234 .

7. Reich, S.; Thomsen, C.; Maultzsch, J. Carbon Nanotubes: An Introduction to the Basic Concepts and Physical Properties, (Wiley- VCH, Weinheim, 2004).

8. Jorio, A.; Pimenta, M. A.; Souza Filho, A. G.; Samsonidze, G. G.; Swan, A. K.; Unlü, M. S.; Goldberg, B. B.; Saito, R.; Dresselhaus, G.; Dresselhaus, M. S. *Phys. Rev. Lett.* **2003**, *90*, 107403.

9. Dresselhaus, M. S.; Dresselhaus, G.; Saito, R.; Jorio, A. *Phys. Rep.* **2005**, *409*, 47–99.

10. Benedict, L. X.; Louie, S. G.; Cohen, M. L. *Phys. Rev. B* **1995**, *52*, 8541.

11. Ajiki, H.; Ando, T. *Physica B* **1994**, *201*, 349–352.

12. Tasaki, S.; Yamabe, T. *Phys. Rev. B* **1998**, *57*, 9301–9318.

13. Maultzsch, J.; Telg, H.; Reich, S.; Thomsen, C. *Phys. Rev. B* **2005**, *72*, 205438 .

14. Corkish, R.; Green, M. A.; Watt, M. E.; Wenham, S. R. Applied Photovoltaics, (Earthscan, Routledge, 2007).

15. Vijayaraghavan, A.; Blatt, S.; Weissenberger, D.; Oron-Carl, M.; Hennrich, F.; Gerthsen, D.; Hahn, H.; Krupke, R. *Nano Lett.* **2007**, *7*, 1556–1560.